

**High entropy alloys towards industrial applications
High-throughput screening and experimental investigation**

Conway, Patrick L.J.; Klaver, T. P.C.; Steggo, Jacob; Ghassemali, Ehsan

DOI

[10.1016/j.msea.2021.142297](https://doi.org/10.1016/j.msea.2021.142297)

Publication date

2022

Document Version

Final published version

Published in

Materials Science and Engineering A

Citation (APA)

Conway, P. L. J., Klaver, T. P. C., Steggo, J., & Ghassemali, E. (2022). High entropy alloys towards industrial applications: High-throughput screening and experimental investigation. *Materials Science and Engineering A*, 830, Article 142297. <https://doi.org/10.1016/j.msea.2021.142297>

Important note

To cite this publication, please use the final published version (if applicable).
Please check the document version above.

Copyright

Other than for strictly personal use, it is not permitted to download, forward or distribute the text or part of it, without the consent of the author(s) and/or copyright holder(s), unless the work is under an open content license such as Creative Commons.

Takedown policy

Please contact us and provide details if you believe this document breaches copyrights.
We will remove access to the work immediately and investigate your claim.



High entropy alloys towards industrial applications: High-throughput screening and experimental investigation

Patrick L.J. Conway^{a,*}, T.P.C. Klaver^b, Jacob Steggo^a, Ehsan Ghassemali^a

^a Department of Materials and Manufacturing, Jönköping University, SE-551 11, Jönköping, Sweden

^b Department of Materials Science and Engineering, Delft University of Technology, Mekelweg 2, 2628CD, Delft, the Netherlands

ARTICLE INFO

Keywords:

High entropy alloys
In situ tension test
Hardening
Stacking-fault energy
CALPHAD

ABSTRACT

Using the Thermo-Calc implementation of the CALPHAD approach, high-throughput screening of the Co–Cr–Fe–Mn–Ni system was implemented to find ‘islands’ of single phase FCC structure within the compositional space in order to reduce the cost of this well-studied alloy system. The screening identified a region centred around $\text{Co}_{10}\text{Cr}_{12}\text{Fe}_{43}\text{Mn}_{18}\text{Ni}_{17}$, reducing the material cost compared to the equiatomic alloy by ~40%. The alloy was experimentally investigated at room and elevated temperatures, including in-situ tensile testing. The alloy was found to possess slightly lower strength compared to the equiatomic alloy at room temperature, however, exhibited excellent thermal strength up to 873K. Deformation twinning was observed after tensile testing at room temperature, primarily attributed to the reduced stacking fault energy (SFE), which was proven by a thermodynamic model for calculating the SFE. The softening behaviour at room temperature can be explained through solid solution hardening (SSH), whereby a modified approach to Labusch’s model was used to calculate the SSH in reported alloys in this study within the Co–Cr–Fe–Mn–Ni system. The modified models for SFE and SSH are proposed to be implemented into high-throughput screening algorithms for accelerated alloy design towards specific mechanical properties.

1. Introduction

1.1. High entropy alloys and compositionally complex alloys

The term High Entropy Alloys (HEAs) was first coined by Yeh et al. [1] in 2004 when multi-principal elements were proposed, mostly limited to equi-molar proportion of elements in the composition [1,2]. Later, Compositionally Complex Alloys (CCAs) was proposed to broaden the definition to non-equiatomic or multi-phase alloys [3]. Since then, there has been significant research into both equiatomic and non-equiatomic compositions as the vast compositional fields are scanned for regions of improved mechanical and other properties.

HEAs and CCAs exhibit an extremely broad spectrum of properties which can include exceptional strength, hardness, cryogenic properties (FCC based HEAs) and high temperature stability, among other promising properties [1,4–13]. However, one of the current challenges that HEAs face, which in turn limits their industrial application, is the cost associated with raw materials. Due to the inherent design approach of multi-principal elements, HEAs/CCAs often result in the use of high quantities of expensive elements such as Co and Ni, drastically

increasing the cost of the alloy. Hence, it is critical to find compositional regions that reduce the quantity of these critical and expensive elements, while maintaining the mechanical properties already reported for current HEAs. An additional benefit of minimising the use of Co is the sustainability issue of Co being a critical raw material [14].

1.2. HEA/CCA design challenges

Research around the Cantor alloy system [2], CoCrFeNiMn , has produced both equiatomic and non-equiatomic alloys. The equiatomic system has been extensively studied, ranging from mechanical properties at cryogenic temperatures [15,16] to dislocation mechanisms and deformation behaviour [17,18]. Thus far, research into the non-equiatomic compositional regions has mainly been focused on improving specific mechanical properties. While there are several non-equiatomic alloys, the unexplored compositional region remains immense. In order to identify these compositional regions of interest, taking a 5 element system with 1 at% increments for each element results in $> 10^6$ possible compositions, which is challenging to investigate experimentally. It is, therefore, necessary to first computationally

* Corresponding author.

E-mail address: patrick.conway@ju.se (P.L.J. Conway).

<https://doi.org/10.1016/j.msea.2021.142297>

Received 30 August 2021; Received in revised form 4 November 2021; Accepted 4 November 2021

Available online 12 November 2021

This is an open access article under the CC BY license (<http://creativecommons.org/licenses/by/4.0/>).

identify optimum compositional spaces, based on design criteria, such as density, mechanical properties, and cost. Accelerating this search can be performed through several approaches, including empirical modelling, first principal simulations, machine learning and high throughput CALPHAD screening, each with various strengths which is reviewed by Li et al. [19]. For broad screening of large compositional spaces with improved accuracy over simplified empirical models, machine learning and CALPHAD predictions offer broad and rapid screening. However, machine learning in HEAs is currently in its infancy and limited by a lack of standardisation of published data and small data sets [19,20]. This study, therefore, focuses on the use of high-throughput CALPHAD screening techniques to identify a compositional region with reduced cost based upon compositional constraints.

The CALPHAD approach for thermodynamic predictions has been used for predicting phase equilibria in multi-component systems, and was first introduced by Kaufman in 1970 [21]. The CALPHAD approach has since been used in the development of HEAs and CCAs with the application of commercial databases such as Pan-HEA (CompuTherm [22]) and TC-HEA (Thermo-Calc [23]). These databases typically use binary and ternary data of known phases from experimental data, resulting in high accuracy at the corners (single element rich regions) of the phase diagrams. This can result in less accurate predictions away from these known areas, and as more experimental data is produced, the databases will become more accurate. Studies have looked at the accuracy of the Thermo-Calc database used in this study (TC-HEA2) and found decent agreement with several experimental studies, with improved accuracy after long-term heat treatments to avoid any metastable phases or casting inhomogeneities [24].

1.3. Mechanical behaviour of HEAs/CCAs

While cost and density, as two examples of alloy design criteria, could be modified using high-throughput screening techniques, predicting the mechanical properties for a wide range of compositions is more complicated. When modifying the composition of HEAs/CCAs, several strengthening mechanisms contribute to the mechanical properties. Two key mechanisms for single phase solid solutions that influence the mechanical properties of HEAs are twinning and solid solution hardening (SSH). The activation of twinning during deformation is known as deformation twinning, which can lead to Twinning Induced Plasticity (TWIP) effect, that influences the deformation behaviour and mechanical properties. While earlier studies highlighted different trends in terms of mechanical properties with the presence of deformation twinning, this was largely due to differences in structural ordering [25–27]. For FCC type alloys such as austenitic steels, deformation twinning typically results in improved fatigue life due to the reduction of strain around deformation twins [28], improved tensile ductility [29], and excellent shock resistance, allowing for high-strain forming processes such as deep drawing and extrusion [30]. Therefore, it would be favourable to be able to design alloys in compositional regions likely to activate deformation twinning.

Twinning is known to be activated by a reduction in the stacking fault energy (SFE), which can be altered by a number of ways, including modification of chemical composition, grain size, strain rate and deformation temperature [31–33]. The SFE can be calculated/measured by several methods, including ab-initio calculations, TEM, XRD, and using thermodynamic models.

In addition to changes in SFE, modification to the composition leads to a change in the amount of SSH in all alloys, including HEAs, which in turn contributes to the change in yield strength. SSH has long been discussed within high entropy alloys, with various methods of determining the extent within these multi-component systems [17,34–36]. Traditionally, the amount of hardening from the introduction of solute atoms to a system is verified through experimental observation of change in strength. However, with the vast possibilities of varying different elements in HEAs, this is simply too time-consuming and

costly. Hence, it would be desirable to have at a minimum, a qualitative method of determining the extent of SSH in multi-component systems. The primary models for SSH are based around the introduction of small solute concentrations to a solute-free lattice [37,38]. Recent work has shown that Labusch's theory for SSH holds for concentrated binary alloys [39].

In this study, the Labusch theory was further modified to account for multi-principle element alloys. A model that can quantitatively predict SSH, along with the prediction for the initiation of deformation twinning, within HEAs/CCAs will facilitate more focused high-throughput screening for targeted mechanical properties and open a new horizon for the design of novel alloys.

By restricting the quantity of expensive elements such as Co and Ni, high throughput screening was used to identify a novel and cheaper non equiatomic high entropy alloy within the Cantor alloy system. This alloy's mechanical properties and deformation mechanisms were investigated at room and elevated temperature (873K) using in-situ tensile testing. The observed microstructural responses during deformation was correlated with existing models and theories. Accordingly, related models calculating the SFE and SSH was modified. The findings are valuable base for further development of modern alloy screening techniques in future, incorporating also models for SFE and SSH to identify new regions of compositional interest for specific applications/properties.

2. Method

2.1. Computational

The alloy was designed by high throughput screening of the Co–Cr–Fe–Mn–Ni system with the method introduced and thoroughly elaborated in Ref. [40]. Element compositions were varied in 1 or 2 at% increments for all five elements, resulting in 1.78 million composition variations. Phases and volume fractions were calculated every 50 K from 500 K to 2500 K, using the TCHEA2.1 thermodynamic database [41,42] within the Thermo-Calc implementation of the CALPHAD method. The Thermo-Calc output was screened for single FCC phases using Matlab. The Matlab code allows for constraints to be imposed. The constraints applied in this study included that each element must be present in ≥ 10 at% concentration to achieve a high entropy of mixing, and additionally, Co and Ni were constrained to have maximum concentrations of 15 and 20 at%, respectively, in order to reduce associated cost.

2.2. Experimental

The selected alloy was produced via arc melting and vacuum casting into a 15×15 mm square copper mould, under a protective Ar atmosphere with high purity elements ($\geq 99.99\%$). The cast ingot was homogenised in two stages, firstly it was hot rolled at 950 °C to a reduction of 65% to consolidate the casting by minimising porosity and breaking down the cast and dendritic structure. Secondly, the rolled ingot was subsequently heat treated at 950 °C for 6 h and water quenched to produce an equiaxed structure. Electrical Discharge Machining (EDM) was used to section tensile pieces for in-situ SEM with the dimensions shown in Fig. 1.

The microstructure was characterised using a Tescan Lyra3 SEM equipped with Electron Backscatter Diffraction (EBSD), scanning transmission electron detector (STEM), Energy Dispersive Spectroscopy (EDS) (by EDAX) for compositional and crystallographic characterisation and a focused ion beam (FIB) for the preparation of lamella samples. Samples were mounted, progressively ground with SiC papers to a grit of 4000, followed by polishing with progressively finer diamond solutions to 0.1 μm suspensions, followed by electropolishing (oxalic acid 10%, 15 V, 5 s). The mechanical properties were characterised by Vickers hardness testing and in-situ tensile testing (Kammrath and Weiss in-situ tensile and heating stage) at both room and elevated temperatures. A

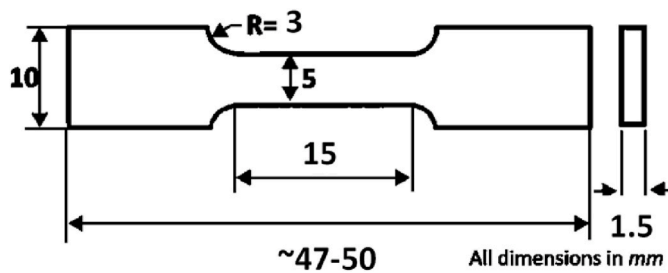


Fig. 1. Dimensions of in-situ tensile specimens, adapted from ASTM E8 standard (subsize dimensions).

Micro-Materials Nanotest system was used for Vickers hardness measurements at a load of 500 g with a loading time of 15 s. The in-situ tensile testing was performed at a displacement rate of 20 $\mu\text{m/s}$ (strain rate = $1.13\text{e}^{-3}\text{s}^{-1}$) on samples that were similarly polished like the samples for microstructural characterisation. It is important to note that due to the relative dimensions of the in-situ stages with respect to the tensile sample size, the strain measurements normally contain experimental error during in-situ tensile testing. This error was minimized in this study by conducting calibration tensile tests using clip-on extensometer on a sample, prior to the actual tensile test. In-situ tensile testing was performed at 293, 723 and 873 K, with a resistive heating unit in contact at the bottom of the tensile specimen, and the temperature was controlled with a thermocouple located between the heating plate and sample. The temperatures were selected based on expected phase transitions and high temperature performance of the alloy, obtained from ThermoCalc calculations. During the tensile test, the loading was paused in order to perform EBSD scans at incremental loads, which you taken from the centre of the tensile specimen. The scans were taken prior to yielding, post yielding, and incrementally up to the ultimate tensile strength (UTS). Lamella samples were prepared by sectioning a $10 \times 1 \mu\text{m}$ rectangle at a depth of 5 μm . The lift-out was progressively ion polished down to <100 nm thickness with the final polish using a beam energy of 5 kV and beam current of 10 pA to remove any amorphous layer.

3. Results and discussion

3.1. Alloy selection

Based upon the high-throughput screening, the centre of a compositional region within the outlined elemental restrictions in Section 2.1 and at 1000K was identified at $\text{Co}_{10}\text{Cr}_{12}\text{Fe}_{43}\text{Mn}_{18}\text{Ni}_{17}$. The ΔS_{mix} for this alloy is calculated to be $1.46R$, where R is the gas constant. This is slightly below the traditional definition of $\Delta S_{\text{mix}} > 1.6R$, and close to the newer definitions of above $1.5R$. The alloy therefore falls into the category of CCAs, or alternatively multi-principal element alloy (MPEA), with the developed screening technique applicable to all the above-mentioned categories. Similar to most alloys within the Cantor alloy system [43], it is worth noting that the single-phase region is metastable at lower temperatures, with ThermoCalc predicting the formation of a BCC phase. Considering the cost of raw materials, the designed alloy is $\sim 40\%$ cheaper than the equiatomic alloy. The difference in cost will naturally fluctuate over time, with the price for individual elements always changing and current market prices can be found from Refs. [44, 45]. It may be argued that compared to the existing advanced steels, the cost is still higher, but using the proposed methodology in this study, the composition can be further refined once experimentally verified, to produce the desired microstructure and mechanical properties at a further reduced cost, which can open new horizons for further alloy development.

The desirable compositional space cannot be visualised in 5-dimensional space; however, the regions of single-phase FCC structure can

be visualised through binary maps of elements. Fig. 2 highlights the compositional regions of interest of binary pairs and shows how the centre of this region shifts in binary space with increasing temperature (black trend line). Further information about the high-throughput code can be found in Ref. [40].

3.2. Microstructure

The alloy after hot rolling and heat treatment, herein after referred to as the homogenised alloy, was found to have single phase FCC structure in agreement with the prediction from Thermo-Calc, containing a relatively high volume fraction of twinned grains at 36 vol%, and average grain size (excluding twins) of $31 \pm 12 \mu\text{m}$. The SEM micrograph, EBSD maps, and EDS maps are presented in Fig. 3(a), Fig. 3(b and c), and Fig. 3 (d-h), respectively. Although segregation was not observed within the grains, slight micro-segregation was identified across a wider scale between Fe, Mn and Ni, whereby Fe was enriched in the cast dendritic structure compared to Mn and Ni enriched in the inter-dendritic structure. This minor micro-segregation is likely due in part to the original cast structure that still partly remains even after rolling and heat treatment. To achieve a better microstructural homogenisation, further reduction during hot rolling could be applied. Porosity was identified throughout the microstructure after the chemical etching process, which was caused by pitting corrosion, and observed as the black spots on the SEM micrograph and EBSD maps in Fig. 3(a and b). The porosity is observed in all EBSD maps within this study.

Compositional analysis through EDS (at. %) of the alloy revealed that the composition was within EDS error to the nominal composition, as presented in Table 1.

3.3. Mechanical properties

The hardness of the homogenised alloy was found to be 125.1 ± 3.4 HV0.5. In literature, there is no direct data for the hardness of the equiatomic alloy with a grain size in the order of 31 μm ; however, a study of the Hall-Petch relationship by Liu et al. [46] in the equiatomic system found a linear relationship of the grain size to the hardness. Using the relationship identified by Liu et al., a hardness of 138 HV is estimated for the equiatomic system, which is marginally greater than the alloy studied in this work.

The tensile behaviours at room and elevated temperatures were studied using in-situ tensile tests. The test at 723 K was selected based on the prediction of ~ 15 vol% BCC phase from Thermo-Calc (BCC phase appear below 757K), which would identify if there was dynamic phase transformation during deformation, or if twinning is activated. The temperature 873 K was selected as a comparison in high temperature properties of this alloy ($\text{Co}_{10}\text{Cr}_{12}\text{Fe}_{43}\text{Mn}_{18}\text{Ni}_{17}$) against the equiatomic alloy, while no phase transformations expected at this temperature.

The tensile properties and strain hardening rate at each temperature are presented in Fig. 4(a) and (b), respectively, with the summarised data in Table 2. The interruptions in the tensile curves are a result of pausing the test to perform EBSD scans. As expected, the greatest strength was achieved at room temperature and is consistent with previous findings within this alloy system [35]. In comparison to the yield strength of 173.4 MPa at 298 K in $\text{Co}_{10}\text{Cr}_{12}\text{Fe}_{43}\text{Mn}_{18}\text{Ni}_{17}$, the equiatomic alloy has as a yield strength of 216 MPa for the same grain size [35]. The increase in yield strength of the equiatomic alloy is consistent with the hardness data, which is attributed to greater solid solution strengthening in the equiatomic alloy, as discussed in later sections. There is an expected decrease in the work hardening rate with increasing temperature, however the flatter slope observed at 298K is attributed to the formation of deformation twins [47].

Tensile testing at elevated temperatures of 723 K and 873 K resulted in an expected drop in both yield strength and elongation. However, the decrease in yield strength from 293 K to 873 K was only 18%, which is far lower than the 46% decrease in yield strength observed in the

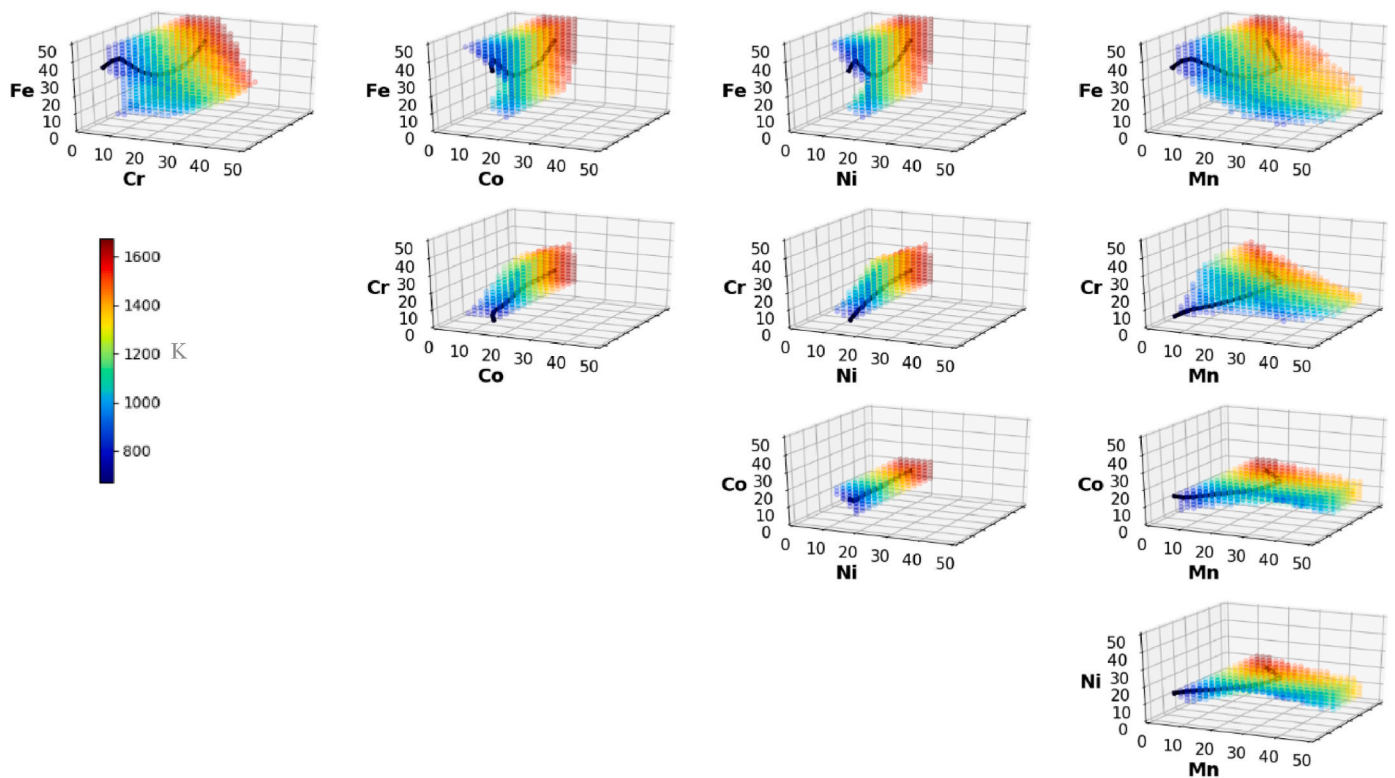


Fig. 2. Regions in binary compositional space (at.%) projected from the 5-element data-set that predict a single phase FCC structure within the specified constraints. Black lines indicate the centre of the compositional space at increasing temperatures.

equiatomic alloy for the same grain size [35], resulting in a greater yield strength at 873K of the new alloy studied here over the equiatomic alloy (142.5 MPa compared to 119.8 MPa respectively). This improved thermal strength is expected to be a contribution of a number of factors, which can be in part due to a change in the contribution of SSH at increased temperatures. While it is feasible to predict the SSH at elevated temperatures through an Arrhenius relation with the activation energy for self-diffusion, the activation energy is typically determined experimentally, with several studies attempting to predict the activation energy show large deviations from experimental values, especially in FCC material [48]. A further study into the activation energy of this alloy compared to other compositions within this system is required in a focused study to identify the contributions to SSH of specific elements at increasing temperatures. To begin understanding the deformation mechanisms at both room and elevated temperatures, the microstructural evolution was evaluated during in-situ testing.

3.4. Microstructural evolution during in-situ tensile

EBSB scans during in-situ testing were performed prior to yielding and post yielding, as well as incrementally until the UTS point (Fig. 4). The incremental scans towards the UTS did not reveal further information, and with surface deformation increasing (Fig. 7), the quality of the EBSB patterns decreased. Fig. 5 presents the specimen before in-situ testing, and during in-situ prior to yielding and post yielding for the tests at 293 K and 723 K. Further analysis of the grain boundaries can be observed in the grain boundary maps presented in Supplementary 1. The test at 723 K revealed an increase in deformation slip. With the increasing temperature, the SFE would further increase, decreasing the possibility of twinning activation [49–52]. The tensile test at 873 K was focused on the mechanical properties; hence no in-situ EBSB is presented at this temperature.

Twinning was confirmed through misorientation maps from the EBSB, which are known to be at a misorientation angle of 60° to the

main crystal orientation in a perfect, undeformed state. The SEM micrograph and corresponding IPF map of the deformed microstructure, highlighting a region with both annealing twins and deformation twins, are presented in Fig. 6(a and b). Fig. 6 (b) shows the difference in orientation between the annealing twins and the newly formed deformation twins within the same grain. This difference in orientation is also confirmed by measuring the misorientation between the grain and the twins. Fig. 6 (c) reveals that the deformation twins have an ideal 60° misorientation angle, compared to a variation of $\pm 10^\circ$ for the annealing twins. This confirms that the annealing twin was present prior to deformation and participated in deformation during tensile loading. This is obvious by the gradual change in the orientation colour throughout the twin (Fig. 6(b)). The deformation twins, on the other hand, are likely formed after significant strain has accumulated and thus they did not have enough time to change orientation during further tensile deformation and thus maintained their characteristic 60° misorientation angle for FCC materials.

During tensile testing, no macro deformation twinning was observed in the EBSB maps, with the only development of twinning occurring during heating and associated with annealing twins, as identified and labelled in Fig. 5(e). However, several grains changed orientation before and after yielding, as labelled in Fig. 5. Fig. 7 presents the same region of the surface after failure, highlighting the reduced slip within these grains compared to the remainder of the alloy. This is attributed to the grains having the most active slip system orientated at an acute angle to the applied stress. This is consistent with previous work suggesting that the dislocation slip is found to be strongly localised within a limited set of slip planes [35,53–55]. This suggests that when the active slip systems are orientated in the direction of load, an increase in slip is favourable. It was further proposed by Otto et al. [35] that the increased slip noticed in the equiatomic alloy was due to the splitting of primary dislocations into Shockley partials with stacking faults in between, ultimately restricting slip to the primary {111} planes.

Furthermore, the absence of macro-deformation twinning is

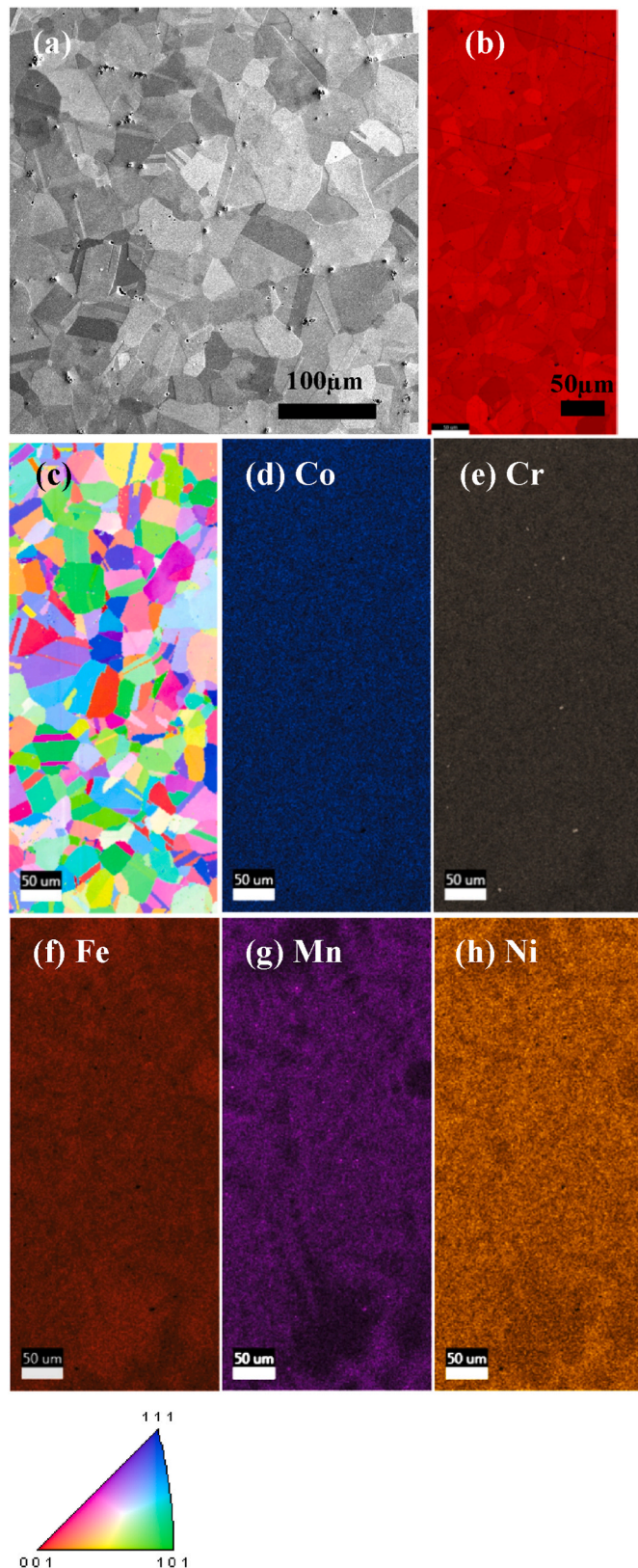


Fig. 3. (a) SEM, (b) phase map (red FCC), (c) Inverse Pole Figure (IPF), and (d-h) EDS maps of $\text{Co}_{10}\text{Cr}_{12}\text{Fe}_{43}\text{Mn}_{18}\text{Ni}_{17}$ after homogenisation. (For interpretation of the references to colour in this figure legend, the reader is referred to the Web version of this article.)

Table 1

EDS composition of $\text{Co}_{10}\text{Cr}_{12}\text{Fe}_{43}\text{Mn}_{18}\text{Ni}_{17}$ in at. %.

	Co	Cr	Fe	Mn	Ni
Nom	10	12	43	18	17
EDS	10.01 \pm 0.2	12.56 \pm 0.4	43.43 \pm 0.2	17.05 \pm 0.6	16.83 \pm 0.8

consistent with alloys in the same family, whereby twinning is not active at room temperature and becomes active at cryogenic temperatures [15, 56,57]. This is regularly attributed to the change in stacking fault energy at lower temperatures [49]. While the SFE can be calculated through extensive computational methods, it is difficult to quickly and accurately calculate with empirical-based methods. However, the effect of elements within specific ternary systems has been studied. From ternary systems, it is suggestive that by decreasing Cr [58] and Ni [58,59], such as in the alloy presented, the SFE will be decreased. However, this is potentially offset by the increase in Fe content which is calculated to increase the SFE in the ternary FeCrNi system [58]. In order to confirm if any deformation twinning was activated (micro/nano), a cross-section of the sample was analysed after the in-situ test (Fig. 8). It was revealed that deformation twins had formed. The scale of these deformation twins was clearly <50 nm wide twins layered when observed in the SEM, to produce twinned regions with a total width of ~2 μm, Fig. 8 (c). However, it is known that the observation of nano twins is often overestimated when measured in SEM or EBSD [60]; hence a lamella of the region with deformation twins was extracted via FIB milling and polished down to <100 nm thick. STEM imaging, Fig. 9, revealed that the size of the deformation twins was ~15 nm. The deformation twins are observed to be curved in several regions, which is a result of continual strain and slip deformation occurring to the bulk material after the deformation twins have formed. This has therefore resulted in plastic deformation of both the primary grains and the deformation twins within the host grain.

3.5. Twinning and stacking fault energy

The presence of deformation twinning in any alloy is of great interest due to the increase in work hardening, resulting in improved elongation, ultimate tensile strength [61], fatigue life and shock resistance [62,63], amongst other properties. Hence, it is critical to understand what has attributed to the formation of deformation twins in the alloy studied here compared to the equiatomic alloy. As forementioned, when increasing the SFE, the primary deformation mechanism changes from HCP transformation to twinning and then to slip. The SFE is not only affected by the composition but also the grain size, temperature, and strain rate [31–33]. The effect of grain size on the activation of twinning has also been identified to occur in HEAs by Sun et al. [56], which suggests an increase in SFE with decreasing grain size. Comparing this study to the equiatomic alloy [35], the grain size in the present study was larger (31 μm compared to 4.4 μm). While it is not known at which grain size the SFE will begin to increase in this system, it is well studied that the SFE in austenitic steels rapidly increases with grain sizes below 35 μm [64], and found that there is an optimum grain size to initiate twinning [65]. This is likely a contributing factor to the formation of deformation twins in this study but would need further investigation into the effect of grain size in this alloy.

The SFE can be calculated or measured in several ways, namely by ab-initio simulations, XRD, TEM or a thermodynamic model. The thermodynamic approach was first proposed by Olson and Cohen [66], and has since been widely used in a wide range of systems [60,67–72]. Due to the interest for high-throughput screening, the thermodynamic approach is used to determine the change in the SFE and is calculated as in Eq. (1):

$$\gamma_{SFE} = 2\rho(\Delta G_m^{T-e} + E_m^{str}) + 2\sigma \quad \text{Eq. 1}$$

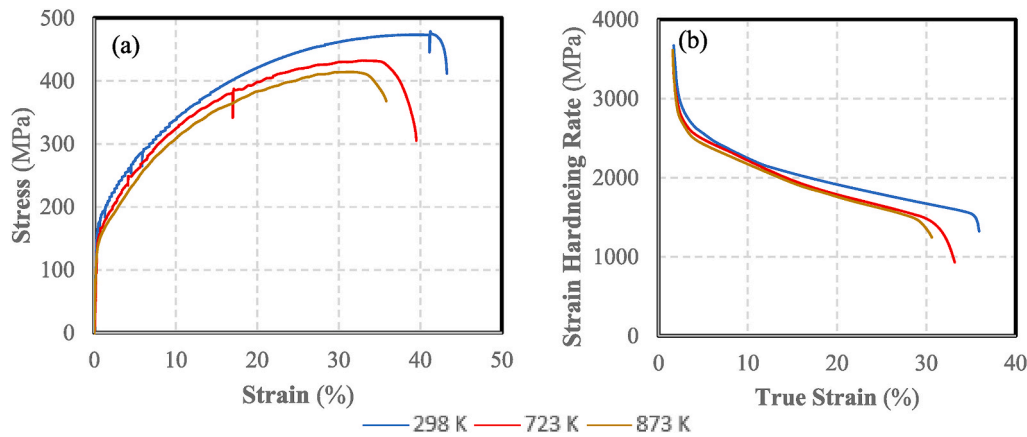


Fig. 4. (a) Engineering stress-strain (tensile) curves and (b) strain hardening rate of $\text{Co}_{10}\text{Cr}_{12}\text{Fe}_{43}\text{Mn}_{18}\text{Ni}_{17}$ at 293, 723 and 873 K during in-situ testing. The interruptions in the curves are EBSD acquisition points.

Table 2

Tensile properties of $\text{Co}_{10}\text{Cr}_{12}\text{Fe}_{43}\text{Mn}_{18}\text{Ni}_{17}$ at 293, 723 and 873 K, compared to the equiatomic composition adjusted to equal grain size [35].

	293 K	723 K	873 K
Yield (MPa)	173.4 ^a [216]	151.9	142.5 ^a [119,8]
UTS (MPa)	478.6	432.4	414.4
Elongation (%)	43.3	39.5	35.8

^a Yield strength in parenthesis of equiatomic alloy at equal grain size.

where ρ is the molar surface density and defined in Eq. (2):

$$\rho = \frac{4}{\sqrt{3}} \frac{1}{a^2 N_A} \quad \text{Eq. 2}$$

$\Delta G_m^{\gamma-\epsilon}$ is the difference in Gibbs free energy between the FCC and HCP phases, as determined by Thermo-Calc. σ is the surface energy, which is typically calculated from experimentally determined data, with a lower surface energy marginally reducing the overall SFE. Reported values for the surface energy are typically in the range of 5–20 mJ m^{-2} , which seems to be a relatively smaller contribution to the SFE than $\Delta G_m^{\gamma-\epsilon}$, hence a common value for Fe–Cr–(Mn–Ni) systems of 10 mJ m^{-2} is applied [60,64,66,67,69,73,74].

E_m^{str} is the strain energy contribution and typically contributes <0.1% to the overall SFE [66]. The elastic strain can be calculated in a number of ways; however, the model by Ferreira and Mullner [67,75], which was applied to austenitic steels, has been used in this work:

$$E_m^{\text{str}} = 2s \frac{G\epsilon^2}{4(1-\nu)} \quad \text{Eq. 3}$$

$$s = \frac{a}{\sqrt{h^2 + k^2 + l^2}} \quad \text{Eq. 4}$$

where G is the shear modulus, ϵ is the contraction along the hcp c-axis, which has been assumed to be -0.02 (2%) based upon work by Tisone [76], and ν is Poisson's ratio, which we have assumed to be constant across the alloys in this system. Although it is likely to vary slightly, the difference between the ideal Poisson's ratio for FCC material, and that measured for the equiatomic alloy differs from 0.261 [77] to 0.259 [16, 78], respectively. A value of 0.259 was taken for this study. The crystallographic system (h, k, l) is the close-packed plane, which is {111} in FCC material.

The SFE for was calculated through the thermodynamic model in Eq. (1), with the Gibbs free energy for individual phases calculated with Thermo-Calc. An example calculation is presented in Supplementary 2, with the contributions from $\Delta G_m^{\gamma-\epsilon}$ considerably larger than the σ and the E_m^{str} as expected and discussed above. The SFE for the alloy studied here

was found to be 57.8 mJ m^{-2} . This is lower than the calculated SFE energy for the equiatomic system of 77.7 mJ m^{-2} , as well as the non-equiatom alloy $\text{Co}_2\text{Cr}_5\text{Fe}_{40}\text{Mn}_{27}\text{Ni}_{26}$ (77.2 mJ m^{-2}) which similarly did not report any deformation twins and the authors attributed this to a potentially higher SFE [79]; although they did not calculate the SFE to confirm this claim. All of these values are greater than the low-to-medium SFE energy required to activate twinning in FCC materials of $\sim 18\text{--}45 \text{ mJ m}^{-2}$ suggested by Curtze et al. [60], and significantly greater than the SFE required for FCC-HCP transformation twinning to occur [80], which was not observed and would not be expected. However, there is known to be an error within the thermodynamic approach to calculating the SFE, which is in part due to the calculated Gibbs free energy for the HCP phase in Thermo-Calc as it is not a stable phase and hence it is not possible to verify these values experimentally. Regardless, the thermodynamic approach does suggest a reduction in SFE for the alloy in this study, which is likely to contribute to the formation of deformation twins during tensile loading. It is also worth noting that the experimentally determined SFE for the equiatomic alloy has been found to be in the range of 18.3–27.3 mJ m^{-2} [49,59], which is less than predicted by the thermodynamic model. This is suggestive that the SFE for $\text{Co}_{10}\text{Cr}_{12}\text{Fe}_{43}\text{Mn}_{18}\text{Ni}_{17}$ could be lower and within the traditional limits for twinning. A conversion factor between the thermodynamic model and the experimental values would prove valuable. While there are experimentally reported values for the SFE of the equiatomic alloy, there is limited data on the SFE for non-equiatom alloys, and any conversion would need more data to generate a statistically accurate conversion factor.

3.6. Solid solution hardening

The change in mechanical properties, softening during tensile testing, at room temperature between the alloy studied here and the equiatomic alloy is not large; however, in the interest of future alloy design, it is prudent to understand the cause and predict this trend across a wider compositional space to accelerate future alloy design. The change in yield strength compared to the equiatomic alloy [35], and in comparison to non-equiatom alloys in literature [79,81,82], a strengthening model is proposed.

The dominant theories in SSH are from Fleischer [37,83] and Labusch [38]. These theories, while similar, do have fundamental differences. Both theories consider the interaction of a dislocation passing by a solute atom, with the difference being that Fleischer considers that the solute atom interacts independently with the dislocation line as a pinning site. At the same time, Labusch takes into account the summation of the solute atoms along the dislocation glide plane. Hence, for concentrated solid solutions, the Labusch model would be expected to be

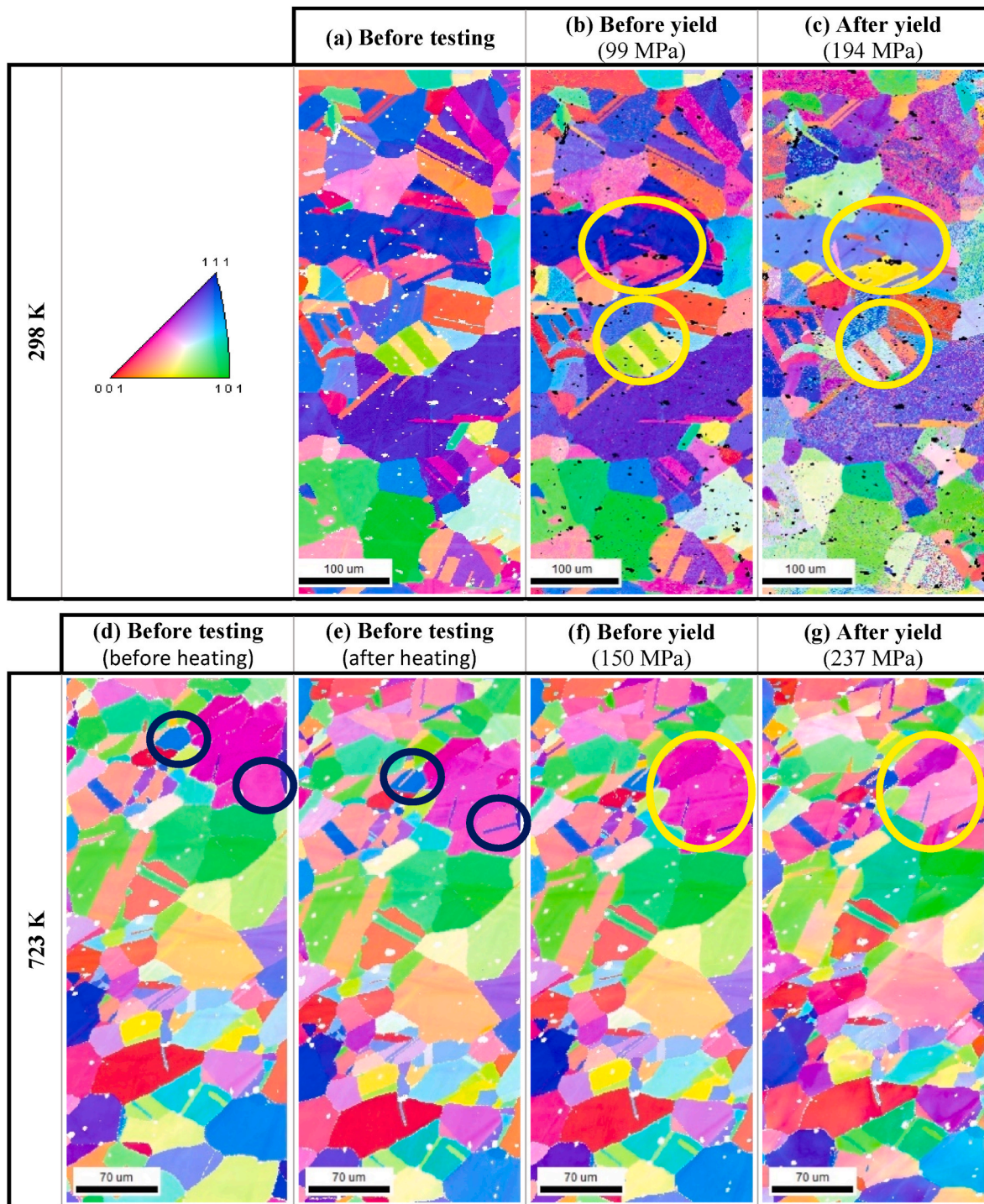


Fig. 5. EBSD maps during in-situ testing at (a–c) 293 K and (d–g) 723 K, before testing (a, d–e), prior to yielding (b, f) and after yielding (c, g). Yellow circles identify grains rotating after yielding, black circles identify the formation of annealing twins upon heating. (For interpretation of the references to colour in this figure legend, the reader is referred to the Web version of this article.)

more applicable. It is important to note that both models do not take into account the effect of thermally activated mechanisms, however this has been shown to be minimal at room temperature and both models describe SSH accurately. Labusch’s model was examined by Kadambi et al. [39], where they studied several binary systems across the entire compositional region and found Labusch’s model to calculate the SSH within the single phase alloys accurately, and the authors further suggested that it could potentially be applied to HEA systems.

Labusch described the change in shear stress for the introduction of a

solute element as:

$$\Delta\tau = Z \cdot G_{SM} \sum_i^n \epsilon_i^{\frac{2}{3}} c_i^{\frac{1}{3}} \tag{Eq. 5}$$

where Z is a constant which is typically used as a fitting parameter that incorporates the dislocation line tension, maximum force for dislocation movement and the Schmid factor, G_{SM} is the shear modulus of the solute free lattice, c is the concentration of i solute atoms, and ϵ is the misfit parameter which consists of misfit contributions from lattice and shear

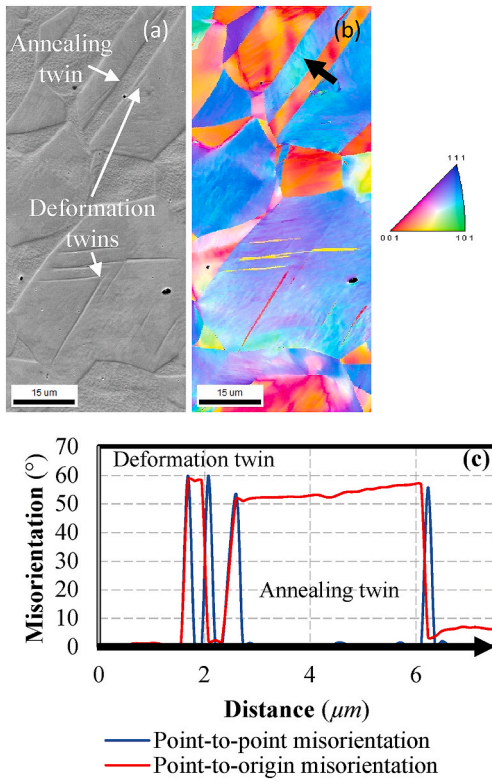


Fig. 6. Annealing and deformation twinning shown in a (a) SEM micrograph and (b) IPF map. (c) Misorientation of the annealing twin and a deformation twin in the direction of the black arrow in the IPF map.

modulus differences, and is defined in Eq. (6):

$$\epsilon = (\epsilon'_{modulus}{}^2 + \alpha^2 \epsilon'_{misfit}{}^2)^{\frac{1}{2}} \quad \text{Eq. 6}$$

where the constant α corresponds to the prominent or lowest energy active dislocation type and is < 16 for screw dislocations (typically close

to 3) and $16 > \alpha > 32$ for edge dislocations depending on the distance of the solute from the shear plane. For a ductile FCC alloy with presumably multiple active slip-systems, the most likely dislocation to occur based on the lowest energy are screw dislocations with a Burgers vector of $a/2 < 110 >$, which is consistent with TEM studies by Okamoto et al. [36]. Hence a value of $\alpha = 3$ is used.

ϵ'_{misfit} describes local lattice distortion due to the solute addition, often determined experimentally by $1/a \cdot da/dc$, where a is the lattice constant without solute additions. This ideally represents the relative change in the perfect Burgers vector due to the solute in the dislocation line.

$\epsilon'_{modulus}$ represents the calculated first-order change in local shear modulus taken from the experimentally measured value of $\partial G/\partial c$ from a bulk sample, and is defined in Eq. (7):

$$\epsilon'_{modulus} = 1 / G \cdot \partial G / \partial c (1 + 1/2 |1/G \cdot \partial G / \partial c|)^{-1} \quad \text{Eq. 7}$$

As a result of Eq. (6), Labusch's model suggests that any difference in the radii or shear modulus of the solute elements will result in a strengthening effect.

In order to determine the effect of solutes on local shear without experimental data, it would require first an approximation of the shear modulus. A recent study by Huang and Vitos [84] examined various elastic parameters in HEAs which included the determination of the shear modulus. Trends between experimentally determined values and empirical calculations were identified via both a simple rule of mixtures of the constituent elements, but also the product of the average electron density at the Wigner-Seitz cell (n_{ws}) by the average atomic volume. Both methods were applied with slightly different values but similar trends; hence, a rule of mixtures of constituent elements was applied to this model for simplicity.

The strengthening model by Labusch was originally proposed and applied to a comparatively low concentrated solution and has later been found to work for concentrated binary systems [39]. However, in order to apply it to HEAs, the starting lattice parameter and shear modulus of the 'solute free' lattice needs to be determined. This can be done by either taking one of the elements as the solvent or by determining an approximation of the lattice parameter and shear modulus in the

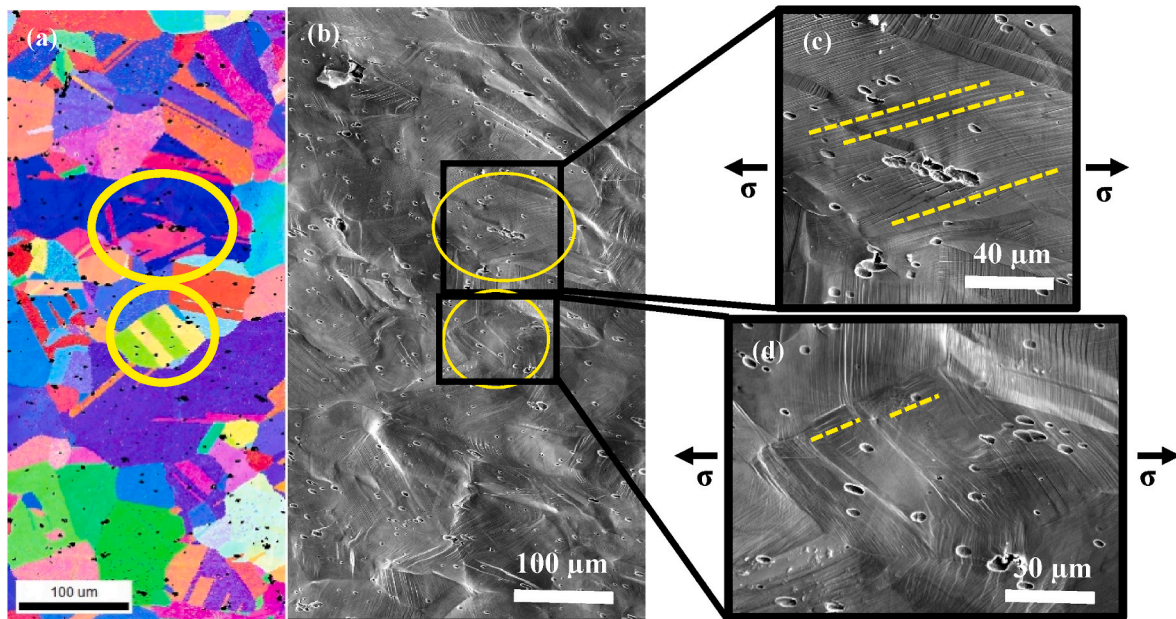


Fig. 7. (a) IPF pole map of the undeformed region compared to (b-d) SEM micrographs after deformation of the same region investigated during in-situ tensile testing at 298 K. The grains which rotated during deformation show reduced slip and an active slip system at an acute angle to the strain direction (yellow dashed lines). (For interpretation of the references to colour in this figure legend, the reader is referred to the Web version of this article.)

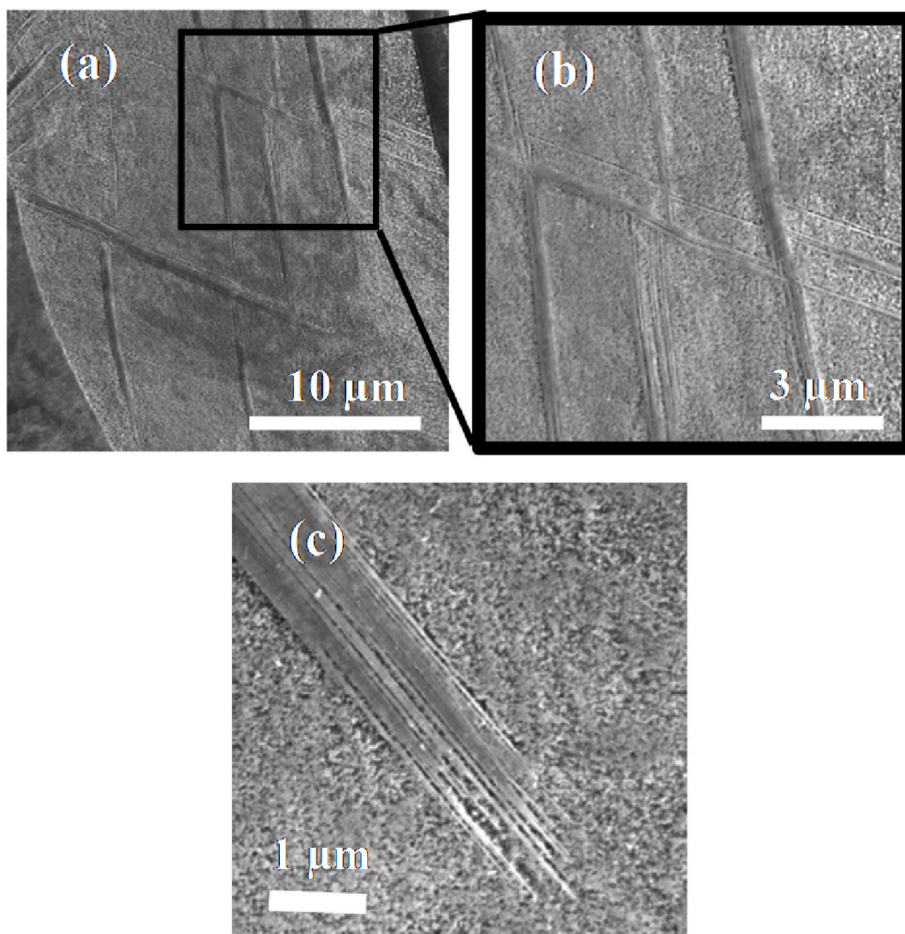


Fig. 8. SEM micrographs of the etched cross-section in the transverse direction after tensile loading. (a–b) Interaction of multiple deformation twins and (c) lamella structure of deformation twins.

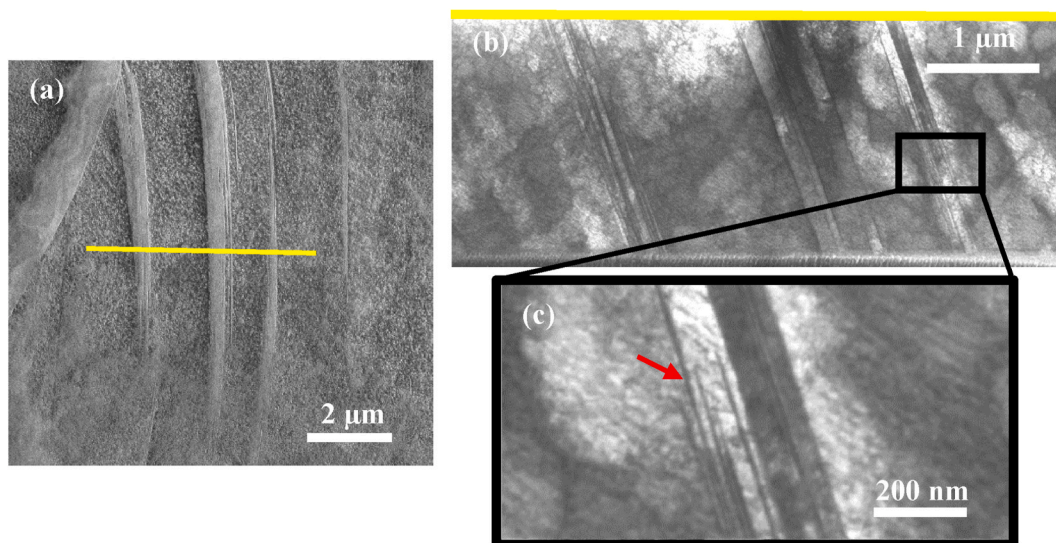


Fig. 9. (a) SEM micrograph of deformation twins that were examined under (b–c) STEM imaging via FIB milling lift out. Example of 15 nm thick nano deformation twin labelled with red arrow. The yellow line identifies the region that was lifted out. (For interpretation of the references to colour in this figure legend, the reader is referred to the Web version of this article.)

multi-component state, and subsequently determining each element from this approximation. When using the first method, depending on which element was used as the solvent, the SSH component was found to

vary by a factor of 2 within the equiatomic alloy, with greater deviation for non-equiatomic alloys. Part of this variation is likely due to the shear modulus of the pure elements from different crystal structures. Hence,

Table 3

Experimentally determined yield strength of alloys within the Co–Cr–Fe–Mn–Ni system, the calculated SSH effect and SFE.

	Yield strength (MPa) ^a	$\Delta\tau$ (Z·GPa)	SFE (mJ.m ⁻²)
Co ₁₀ Cr ₁₂ Fe ₄₃ Mn ₁₈ Ni ₁₇	173.4	0.44	57.8 ^e
CoCrFeMnNi [35]	216 ^a	0.56	77.7
Co ₅ Cr ₂ Fe ₄₀ Mn ₂₇ Ni ₂₆ [79]	94 ^b (GS45μm)	0.40	77.2
Co ₃₅ Cr ₂₀ Fe ₁₅ Mn ₁₅ Ni ₁₅ [81]	231 ^b (GS16.3μm)	0.55	67.4 ^c
Co ₃₅ Cr ₂₅ Fe ₁₀ Mn ₁₅ Ni ₁₅ [81]	305 ^b (GS11.2μm)	0.59	42.0 ^c
Co _{5.9} Cr _{2.3} Fe _{42.2} Mn _{20.7} Ni _{28.9} [82]	123 ^b (GS36.5μm)	0.41	101.6
Co _{5.5} Cr _{2.2} Fe _{41.1} Mn _{24.1} Ni _{27.1} [82]	117 ^b (GS42.7μm)	0.40	87.4
Co _{5.2} Cr _{2.1} Fe ₄₀ Mn ₂₇ Ni _{25.7} [82]	121 ^b (GS32.3μm)	0.39	76.9
Co _{5.8} Cr _{2.4} Fe _{29.4} Mn _{33.9} Ni _{28.5} [82]	139 ^b (GS33μm)	0.43	77.4
Co _{5.8} Cr _{2.4} Fe _{25.7} Mn _{37.6} Ni _{28.5} [82]	135 ^b (GS26.4μm)	0.43	75.5

^dAdjusted to account for grain size.^a Adjusted to the grain size of 31 μm.^b Various grain size, in parenthesis.^c Calculated based on one SEM image from [79].^e Deformation twinning observed.

determining an approximation of the lattice parameter and shear modulus in the multi-component state is required so that the solute free lattice is considered as the average of the constituent elements, and all elements are considered solutes elements changing this average. As forementioned, a rule of mixtures is sufficient for predicting the shear modulus; however, the lattice parameter also needs to be predicted. It has been long postulated that a rule of mixtures result is a good approximation of the lattice parameter [85], with early studies measuring the lattice parameter with additions up to 100 at.% solute atoms revealing a linear trend [85–87]. This same trend is also observed in many systems up to the point of phase boundaries [88]. Several studies of HEAs report close agreement between measured lattice parameters and a rule of mixtures from the atomic radii [89–91]. In order to corroborate the validity of this, a further comparison was made for alloys where XRD data was reported for alloys within the Cantor system [79,82,92,93] to a rule of mixtures, with the largest deviations of 0.8% (equivalent to 0.02 Å) in the highest Mn containing alloy studied by Pradeep et al. [82], and an average of 0.3% (0.0014 Å). Variations to the rule of mixture are known to exist, and partly due to electronic interactions of the outer quantum shell [88]. This can be predicted via quantum physics; however, it is beyond the scope of a high throughput screening technique developed here. For the sake of simplicity and accuracy for high throughput screening for mechanical properties, the accuracy of a rule of mixture is considered sufficient to highlight trends across the compositional space.

With the approximation for the shear modulus, Eq. (5) becomes modified from G_{SM} to G_{avg} . The ϵ'_{misfit} from Eq. (6) can be calculated from the average radius of constituent elements as $a_{avg} = 4r_{avg}/\sqrt{2}$. The effect of a substitutional solute atom in the unit cell can be determined as $a_{sol} = (2r_{sol} + 2r_{avg})/\sqrt{2}$. Hence, the effect of the solute atom in the cell is defined as $(a_{sol} - a_{avg})/a_{avg}$. Finally, the $\epsilon'_{modulus}$ is calculated from a change in the shear modulus to the average modulus. The constant Z in Eq. (5) is treated as constant across the alloy system revealing the shift in SSH as a factor of this constant across the compositional region. This removes any data fitting inconsistencies; however, does mean that these values cannot be directly compared to different alloy systems and instead used to identify SSH trends within the same alloy system. An example calculation is presented in Supplementary 3.

This model will estimate the contribution of SSH to the shear strength. The calculated contributions to the shear strength for a selection of reported HEAs within the CoCrFeMnNi system, alongside the measured yield strength (adjusted via the Hall-Petch relationship), are presented in Table 3. Naturally, the strength attributed from the individual elements needs to be taken into consideration to match with the experimental data, which would be required to calculate the final yield strength of the alloy due to the changing base shear strength (τ_0). This would require heavy computational modelling to understand the base

strength of individual elements for the host crystal structure, which is beyond the scope of this model and limits the model to known compositional regions. However, examining the change in the experimentally determined yield strength and change in the calculated $\Delta\tau$ of the listed alloys to the equiatomic alloy after grain size adjustment, the model shows excellent agreement across all alloys as seen in Fig. 10. While the deviations from the trend line can reasonable be assumed to come partly from a shift in τ_0 , the agreement highlights the tremendous potential use when screening the ‘islands’ of compositions for regions of desirable mechanical properties.

3.7. Future direction for alloy design

With multiple factors directing possible alloy design, selections must be made on which compositional direction from the current alloy will yield the most favourable change in mechanical properties. Fig. 11 highlights the optimal directions from the composition of the alloy studied here (circle) to the optimal alloy composition (red star) for an increase in SSH (Fig. 11(a)) and decrease in SFE (Fig. 11(b)).

In the case of increasing SSH, an increase in SSH is observed in any direction of increasing Cr, Mn or Ni, with the largest increase in the Cr rich direction. While maintaining Co at 10 at.%, the maximum SSH on the pseudo quaternary is seen at Co₁₀Cr₄₀Fe₀Mn₄Ni₄₆ (Fig. 11 (b)),

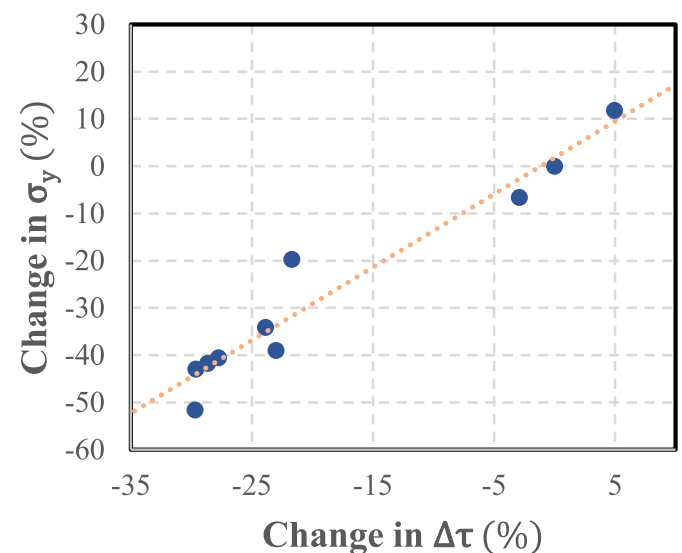


Fig. 10. Change in experimentally determined yield strength against the calculated change in SSH ($\Delta\tau$) with reference to the equiatomic alloy. All alloys are compared to the equiatomic alloy with equivalent grain size.

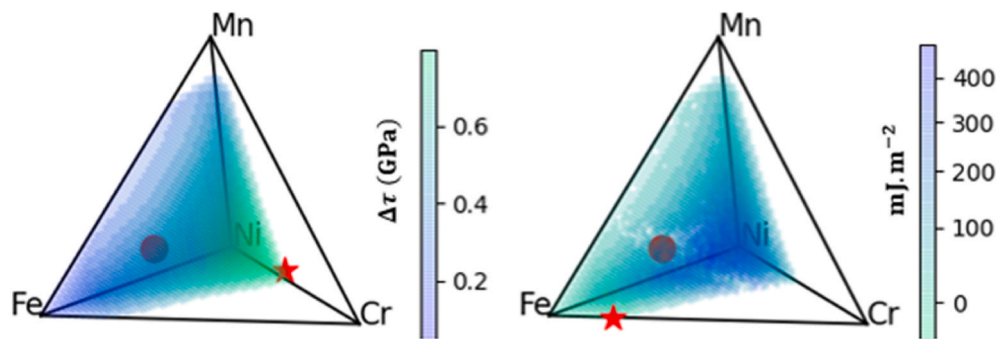


Fig. 11. Quaternary diagrams at 10 at.% Co identifying the location of the alloy studied here (circle) and the optimum composition (red star) for (a) maximising SSH and (b) minimising SFE. (For interpretation of the references to colour in this figure legend, the reader is referred to the Web version of this article.)

however, while maintaining ≥ 40 at.% Fe in order to reduce the cost of the overall alloy and ≥ 10 at.% of constituent elements for the high entropy concept, the maximum SSH is in the direction of $\text{Co}_{10}\text{Cr}_{20}\text{Fe}_{40}\text{Mn}_{10}\text{Ni}_{20}$. Maintaining Co in the alloy will always result in an increased alloy cost, with recent work studying Co-free medium entropy alloys studying the mechanical performance of these alloys [94,95]. By releasing the restriction on Co, both the cost can be decreased with a predicted increase in SSH; hence an alloy that has a maximised SSH with Co and an alternative without Co is suggested for future study. A summary of suggested alloy directions and the corresponding change in shear stress is presented in Table 4. Utilising the trend between the change in yield strength and change in $\Delta\tau$ presented in Fig. 10, the yield strength of the newly proposed alloys is also predicted. The strength of single-phase alloys will primarily be limited by grain size refinement and solid solution strengthening, and in order to further maximise the mechanical performance of HEAs/CCAs, additional strengthening mechanisms will need to be applied once the matrix properties are maximised, such as microstructure refinements or secondary phases [96, 97].

Reducing the SFE, and hence promoting activation of deformation twinning, the lowest SFE is observed at a composition of $\text{Fe}_{72}\text{Cr}_{18}\text{Co}_{10}\text{Ni}_0\text{Mn}_0$ (SFE -25.53 mJ m^{-2}) within the compositional island presented in the pseudo quaternary diagram, with the lowest at $\text{Fe}_{56}\text{Cr}_{14}\text{Co}_{10}\text{Ni}_{10}\text{Mn}_{10}$ (SFE 32.72 mJ m^{-2}) when we take into account the same considerations for maintaining $\text{Fe} \geq 40$ at.% and the remainder of the constituent elements ≥ 10 at.%. It is observed that an increase in Ni and Cr content increases the SFE, which is consistent with experimental observations [58,59].

4. Conclusion

This research designed an alloy within the CoCrFeMnNi system based on high-throughput screening of CALPHAD predictions. The alloy that was designed, produced and studied, $\text{Co}_{10}\text{Cr}_{12}\text{Fe}_{43}\text{Mn}_{18}\text{Ni}_{17}$, had the goal of applying constraints to the expensive elements, Co and Ni, in order to address the barrier of high cost, which limit the industrialisation of HEAs and CCAs. The cost was calculated as a reduction by $\sim 40\%$, with the new alloy resulting in slightly softer mechanical properties compared to the equiatomic alloy at room temperature. However, it showed improved thermal strength with increased strength at elevated temperatures.

Deformation twinning was identified at room temperature in $\text{Co}_{10}\text{Cr}_{12}\text{Fe}_{43}\text{Mn}_{18}\text{Ni}_{17}$, which was attributed to a decrease in the SFE, as calculated via a thermodynamic model and compared to alloys within the same system. The model was found to overestimate experimentally determined values for SFE; however, only alloys with SFE below 67 mJ m^{-2} showed deformation twinning.

The softening at room temperature was proposed to occur due to reduced solid solution hardening with the application of Labusch's theory on SSH modified to apply to concentrated alloys with no base

Table 4

Future alloy design direction based on maximising SSH and minimising SFE as discussed in Section 3.7, with the predicted yield strength based on correlation between the experimentally determined yield strength and the calculated $\Delta\tau$. Comparison to the alloy reported in this study and the equiatomic alloy.

	SSH ($\Delta\tau$) Z-GPa	SFE (mJ. m^{-2})	Cost/ Kg (USD)	Density (G/cm^3)	Predicted σ_y^a (MPa)
$\text{Co}_{10}\text{Cr}_{12}\text{Fe}_{43}\text{Mn}_{18}\text{Ni}_{17}$	0.44	57.8	7.28	8.42	–
CoCrFeMnNi	0.56	77.7	11.67	8.06	–
$\text{Co}_{10}\text{Cr}_{40}\text{Fe}_0\text{Mn}_4\text{Ni}_{46}$	0.79	95.6	13.51	8.15	356
$\text{Co}_{10}\text{Cr}_{20}\text{Fe}_{40}\text{Mn}_{10}\text{Ni}_{20}$	0.51	89.6	8.29	8.0	190
$\text{Co}_{10}\text{Cr}_{18}\text{Fe}_{72}\text{Mn}_0\text{Ni}_0$	0.26	-25.5	5.28	7.85	41
$\text{Co}_{10}\text{Cr}_{14}\text{Fe}_{56}\text{Mn}_{10}\text{Ni}_{10}$	0.39	32.7	6.41	7.94	118
$\text{Co}_4\text{Cr}_{22}\text{Fe}_{40}\text{Mn}_{10}\text{Ni}_{24}$	0.53	74.8	7.07	7.96	202
$\text{Co}_0\text{Cr}_{20}\text{Fe}_{40}\text{Mn}_{10}\text{Ni}_{30}$	0.53	97.2	6.4	8.0	202
$\text{Co}_0\text{Cr}_{42}\text{Fe}_{40}\text{Mn}_{10}\text{Ni}_8$	0.49	22.9	5.41	7.62	178

^a With a grain size of $31 \mu\text{m}$.

solvent element. This model was shown to be consistent with other non-equiatomc alloys within the same system.

It is proposed that future screening for “budget” HEAs/CCAs should include the proposed strengthening model to identify regions of mechanically superior alloys, as well as applying the thermodynamic model for SFE to find alloys where twinning is activated and more populated throughout the material. Several compositional directions were suggested in the study.

CRedit authorship contribution statement

Patrick L.J. Conway: Conceptualization, Methodology, Software, Investigation, Data curation, Writing – original draft, Writing – review & editing, Visualization. **T.P.C. Klaver:** Conceptualization, Software, Methodology, Writing – review & editing. **Jacob Steggo:** Methodology, Software. **Ehsan Ghassemali:** Conceptualization, Methodology, Investigation, Writing – original draft, Writing – review & editing, Funding acquisition, Supervision.

Declaration of competing interest

The authors declare that they have no known competing financial interests or personal relationships that could have appeared to influence the work reported in this paper.

Acknowledgements

The authors would like to thank Kevin Laws from UNSW Sydney for assistance in the production of the alloy, Johan Börjesson from Jönköping University for his support with STEM imaging, and Marcel Sluiter from TU Delft for the idea and discussions of a ‘budget HEA’

which led to this research. This research was partially carried out under the financial support provided by the strategic innovation program for lightweight (LIGHTer), a joint venture by VINNOVA, Formas and the Swedish Energy Agency (NOVELA project, Dia. No. 2019–02624).

Appendix A. Supplementary data

Supplementary data to this article can be found online at <https://doi.org/10.1016/j.msea.2021.142297>.

Data availability

The raw data required to reproduce these findings are available to download from <https://doi.org/10.17632/53wr5f6wfy.1>. The processed data required to reproduce these findings are available to download from <https://doi.org/10.17632/53wr5f6wfy.1>.

References

- J.W. Yeh, S.K. Chen, S.J. Lin, J.Y. Gan, T.S. Chin, T.T. Shun, C.H. Tsau, S.Y. Chang, Nanostructured high-entropy alloys with multiple principal elements: novel alloy design concepts and outcomes, *Adv. Eng. Mater.* 6 (2004) 299–303.
- B. Cantor, I.T.H. Chang, P. Knight, A.J.B. Vincent, Microstructural development in equiatomic multicomponent alloys, *Mater. Sci. Eng.* 375–377 (2004) 213–218, <https://doi.org/10.1016/j.msea.2003.10.257>.
- D.B. Miracle, O.N. Senkov, A critical review of high entropy alloys and related concepts, *Acta Mater.* 122 (2017) 448–511, <https://doi.org/10.1016/j.actamat.2016.08.081>.
- J.W. Yeh, Y.L. Chen, S.J. Lin, S.K. Chen, High-entropy alloys – a new era of exploitation, *Mater. Sci. Forum* 560 (2007) 1–9.
- M.-R. Chen, S.-J. Lin, J.-W. Yeh, M.-H. Chuang, S.-K. Chen, Y.-S. Huang, Effect of vanadium addition on the microstructure, hardness, and wear resistance of Al_{0.5}CoCrCuFeNi high-entropy alloy, *Metall. Mater. Trans.* 37 (2006) 1363–1369, <https://doi.org/10.1007/s11661-006-0081-3>.
- J.-M. Wu, S.-J. Lin, J.-W. Yeh, S.-K. Chen, Y.-S. Huang, H.-C. Chen, Adhesive wear behavior of Al_{0.5}CoCrCuFeNi high-entropy alloys as a function of aluminum content, *Wear* 261 (2006) 513–519, <https://doi.org/10.1016/j.wear.2005.12.008>.
- P.K. Huang, J.W. Yeh, T.T. Shun, S.K. Chen, Multi-principal-element alloys with improved oxidation and wear resistance for thermal spray coating, *Adv. Eng. Mater.* 6 (2004) 74–78, <https://doi.org/10.1016/j.msea.2004.03.005>.
- K.B. Zhang, Z.Y. Fu, J.Y. Zhang, J. Shi, W.M. Wang, H. Wang, Y.C. Wang, Q. J. Zhang, Annealing on the structure and properties evolution of the CoCrFeNiCuAl high-entropy alloy, *J. Alloys Compd.* 502 (2010) 295–299, <https://doi.org/10.1016/j.jallcom.2009.11.104>.
- T.-T. Shun, Y.-C. Du, Age hardening of the Al_{0.3}CoCrFeNiCo_{0.1} high entropy alloy, *J. Alloys Compd.* 478 (2009) 269–272, <https://doi.org/10.1016/j.jallcom.2008.12.014>.
- W.-R. Wang, W.-L. Wang, S.-C. Wang, Y.-C. Tsai, C.-H. Lai, J.-W. Yeh, Effects of Al addition on the microstructure and mechanical property of Al_xCoCrFeNi high-entropy alloys, *Intermetallics* 26 (2012) 44–51, <https://doi.org/10.1016/j.intermet.2012.03.005>.
- C.-J. Tong, M.-R. Chen, J.-W. Yeh, S.-J. Lin, S.-K. Chen, T.-T. Shun, S.-Y. Chang, Mechanical performance of the Al_xCoCrCuFeNi high-entropy alloy system with multiprincipal elements, *Metall. Mater. Trans.* 36 (2005) 1263–1271, <https://doi.org/10.1007/s11661-005-0218-9>.
- K.B. Zhang, Z.Y. Fu, J.Y. Zhang, W.M. Wang, H. Wang, Y.C. Wang, Q.J. Zhang, J. Shi, Microstructure and mechanical properties of CoCrFeNiTiAlx high-entropy alloys, *Mater. Sci. Eng.* 508 (2009) 214–219, <https://doi.org/10.1016/j.msea.2008.12.053>.
- Y.P. Wang, B.S. Li, M.X. Ren, C. Yang, H.Z. Fu, Microstructure and compressive properties of AlCrFeCoNi high entropy alloy, *Mater. Sci. Eng.* 491 (2008) 154–158, <https://doi.org/10.1016/j.msea.2008.01.064>.
- CRM Alliance - Critical Raw Materials, <https://www.crmalliance.eu/critical-raw-materials>.
- W. Huo, F. Fang, H. Zhou, Z. Xie, J. Shang, J. Jiang, Remarkable strength of CoCrFeNi high-entropy alloy wires at cryogenic and elevated temperatures, *Scripta Mater.* 141 (2017) 125–128, <https://doi.org/10.1016/j.scriptamat.2017.08.006>.
- A. Haglund, M. Koehler, D. Catoor, E.P. George, V. Keppens, Polycrystalline elastic moduli of a high-entropy alloy at cryogenic temperatures, *Intermetallics* 58 (2015) 62–64, <https://doi.org/10.1016/j.intermet.2014.11.005>.
- I. Basu, J.T.M. De Hosson, Strengthening mechanisms in high entropy alloys: fundamental issues, *Scripta Mater.* 187 (2020) 148–156, <https://doi.org/10.1016/j.scriptamat.2020.06.019>.
- M. Feuerbacher, Dislocations and deformation microstructure in a B2-ordered Al₂₈Co₂₀Cr₁₁Fe₁₅Ni₂₆ high-entropy alloy, *Sci. Rep.* 6 (2016) 29700, <https://doi.org/10.1038/srep29700>.
- R. Li, L. Xie, W.Y. Wang, P.K. Liaw, Y. Zhang, High-throughput calculations for high-entropy alloys: a brief review, *Front. Mater.* 7 (2020) 290.
- D.Q. Zhao, S.P. Pan, Y. Zhang, P.K. Liaw, J.W. Qiao, Structure prediction in high-entropy alloys with machine learning, *Appl. Phys. Lett.* 118 (2021) 231904, <https://doi.org/10.1063/5.0051307>.
- L. Kaufman, H. Bernstein, *Computer Calculation of Phase Diagrams: With Special Reference to Refractory Metals*, Academic Press, 1970.
- CompuTherm, 2021. June 10, https://compuTherm.com/?path=59_83&route=product%2Fcategory.
- J.-O. Andersson, T. Helander, L. Höglund, P. Shi, B. Sundman, Thermo-Calc & DICTRA, computational tools for materials science, *Calphad* 26 (2002) 273–312, [https://doi.org/10.1016/S0364-5916\(02\)00037-8](https://doi.org/10.1016/S0364-5916(02)00037-8).
- J.E. Saal, I.S. Berglund, J.T. Sebastian, P.K. Liaw, G.B. Olson, Equilibrium high entropy alloy phase stability from experiments and thermodynamic modeling, *Scripta Mater.* 146 (2018) 5–8, <https://doi.org/10.1016/j.scriptamat.2017.10.027>.
- M.H. Yoo, C.L. Fu, J.K. Lee, Deformation twinning in metals and ordered intermetallics-Ti and Ti-aluminides, *J. Phys. III Fr.* 1 (1991) 1065–1084, <https://doi.org/10.1051/jp3:1991172>.
- S. Mahajan, D.F. Williams, Deformation twinning in metals and alloys, *Int. Metall. Rev.* 18 (1973) 43–61, <https://doi.org/10.1179/imtr.1973.18.2.43>.
- H.C. Rogers, J.P. Hirth, R.E. Reed-Hill, in: R.E. Reed-Hill, J.P. Hirth, H.C. Rogers (Eds.), *U. of F. Conference on Deformation Twinning 1963*, Gordon and Breach Science Publishers, New York, 1964. U. of F.M.R. Laboratory., M.S. of AIME., P.M. Committee., Deformation twinning; proceedings.
- J.M. Han, C.Y. Lim, Y.G. Kim, The role of deformation twinning on mechanical properties of an austenitic Fe₃₀Mn_{1.2}Al_{0.3}C alloy, *Acta Metall. Mater.* 39 (1991) 2169–2175, [https://doi.org/10.1016/0956-7151\(91\)90186-5](https://doi.org/10.1016/0956-7151(91)90186-5).
- K. Sato, M. Ichinose, Y. Hirotsu, Y. Inoue, Effects of deformation induced phase transformation and twinning on the mechanical properties of austenitic Fe-Mn-Al alloys, *ISIJ Int.* 29 (1989) 868–877, <https://doi.org/10.2355/isijinternational.29.868>.
- O. Grässel, G. Frommeyer, Effect of martensitic phase transformation and deformation twinning on mechanical properties of Fe–Mn–Si–Al steels, *Mater. Sci. Technol.* 14 (1998) 1213–1217, <https://doi.org/10.1179/mst.1998.14.12.1213>.
- J. Li, J.Y. Zhang, L. Jiang, P. Zhang, K. Wu, G. Liu, J. Sun, Twinning/detwinning-mediated grain growth and mechanical properties of free-standing nanotwinned Ni foils: grain size and strain rate effects, *Mater. Sci. Eng.* 628 (2015) 62–74, <https://doi.org/10.1016/j.msea.2015.01.015>.
- G.H. Xiao, N.R. Tao, K. Lu, Effects of strain, strain rate and temperature on deformation twinning in a Cu–Zn alloy, *Scripta Mater.* 59 (2008) 975–978, <https://doi.org/10.1016/j.scriptamat.2008.06.060>.
- M.A. Meyers, O. Vöhringer, V.A. Lubarda, The onset of twinning in metals: a constitutive description, *Acta Mater.* 49 (2001) 4025–4039, [https://doi.org/10.1016/S1359-6454\(01\)00300-7](https://doi.org/10.1016/S1359-6454(01)00300-7).
- C. Varvenne, G.P.M. Leyson, M. Ghazisaeidi, W.A. Curtin, Solute strengthening in random alloys, *Acta Mater.* 124 (2017) 660–683, <https://doi.org/10.1016/j.actamat.2016.09.046>.
- F. Otto, A. Dlouhý, C. Somsen, H. Bei, G. Eggeler, E.P. George, The influences of temperature and microstructure on the tensile properties of a CoCrFeMnNi high-entropy alloy, *Acta Mater.* 61 (2013) 5743–5755, <https://doi.org/10.1016/j.actamat.2013.06.018>.
- N.L. Okamoto, S. Fujimoto, Y. Kambara, M. Kawamura, Z.M.T. Chen, H. Matsunoshita, K. Tanaka, H. Inui, E.P. George, Size effect, critical resolved shear stress, stacking fault energy, and solid solution strengthening in the CrMnFeCoNi high-entropy alloy, *Sci. Rep.* 6 (2016) 35863, <https://doi.org/10.1038/srep35863>.
- R.L. Fleischer, Substitutional solution hardening, *Acta Metall.* 11 (1963) 203–209, [https://doi.org/10.1016/0001-6160\(63\)90213-X](https://doi.org/10.1016/0001-6160(63)90213-X).
- R. Labusch, A statistical theory of solid solution hardening, *Phys. Status Solidi* 41 (1970) 659–669, <https://doi.org/10.1002/pssb.19700410221>.
- S.B. Kadambi, V.D. Divya, U. Ramamurty, Evaluation of solid-solution hardening in several binary alloy systems using diffusion couples combined with nanoindentation, *Metall. Mater. Trans.* 48 (2017) 4574–4582, <https://doi.org/10.1007/s11661-017-4250-3>.
- T.P.C. Klaver, D. Simonovic, M.H.F. Sluiter, Brute force composition scanning with a CALPHAD database to find low temperature body centered cubic high entropy alloys, *Entropy* 20 (2018) 911, <https://doi.org/10.3390/e20120911>.
- H. Mao, H.-L. Chen, Q. Chen, TCHEAL1: a thermodynamic database not limited for “high entropy” alloys, *J. Phase Equilibria Diffus.* 38 (2017) 353–368, <https://doi.org/10.1007/s11669-017-0570-7>.
- H.-L. Chen, H. Mao, Q. Chen, Database development and Calphad calculations for high entropy alloys: challenges, strategies, and tips, *Mater. Chem. Phys.* 210 (2018) 279–290, <https://doi.org/10.1016/j.matchemphys.2017.07.082>.
- F. Otto, A. Dlouhý, K.G. Pradeep, M. Kuběnová, D. Raabe, G. Eggeler, E.P. George, Decomposition of the single-phase high-entropy alloy CrMnFeCoNi after prolonged anneals at intermediate temperatures, *Acta Mater.* 112 (2016) 40–52, <https://doi.org/10.1016/j.actamat.2016.04.005>.
- Preismonitor - Federal Institute for Geosciences and Natural Resources. https://www.bgr.bund.de/DE/Themen/Min_rohstoffe/Produkte/Preisliste/pm_19_12.pdf (accessed January 12 2021).
- Shan Tang, (Pig Iron) - Shanghai Metals Market, 2021. <https://www.metal.com/Pig-Iron/201808140002>. (Accessed 12 January 2021).
- W.H. Liu, Y. Wu, J.Y. He, T.G. Nieh, Z.P. Lu, Grain growth and the Hall–Petch relationship in a high-entropy FeCrNiCoMn alloy, *Scripta Mater.* 68 (2013) 526–529, <https://doi.org/10.1016/j.scriptamat.2012.12.002>.
- D. Wei, X. Li, S. Schönecker, J. Jiang, W.-M. Choi, B.-J. Lee, H.S. Kim, A. Chiba, H. Kato, Development of strong and ductile metastable face-centered cubic single-phase high-entropy alloys, *Acta Mater.* 181 (2019) 318–330, <https://doi.org/10.1016/j.actamat.2019.09.050>.

- [48] S.Y. Davydov, Calculation of the activation energy for surface self-diffusion of transition-metal atoms, *Phys. Solid State* 41 (1999) 8–10, <https://doi.org/10.1134/1.1130717>.
- [49] S. Huang, W. Li, S. Lu, F. Tian, J. Shen, E. Holmström, L. Vitos, Temperature dependent stacking fault energy of FeCrCoNiMn high entropy alloy, *Scripta Mater.* 108 (2015) 44–47, <https://doi.org/10.1016/j.scriptamat.2015.05.041>.
- [50] J. Wan, S. Chen, Z. Xu, The influence of temperature on stacking fault energy in Fe-based alloys, *Sci. China Ser. E Technol. Sci.* 44 (2001) 345–352, <https://doi.org/10.1007/BF02916685>.
- [51] L. Rémy, A. Pineau, B. Thomas, Temperature dependence of stacking fault energy in close-packed metals and alloys, *Mater. Sci. Eng.* 36 (1978) 47–63, [https://doi.org/10.1016/0025-5416\(78\)90194-5](https://doi.org/10.1016/0025-5416(78)90194-5).
- [52] A.W. Ruff, L.K. Ives, On the temperature dependence of stacking fault energy in cubic and hexagonal silver–tin alloys, *Phys. Status Solidi* 16 (1973) 133–149, <https://doi.org/10.1002/pssa.2210160115>.
- [53] V. Gerold, H.P. Karnthaler, On the origin of planar slip in f.c.c. alloys, *Acta Metall.* 37 (1989) 2177–2183, [https://doi.org/10.1016/0001-6160\(89\)90143-0](https://doi.org/10.1016/0001-6160(89)90143-0).
- [54] J. Olfe, H. Neuhäuser, Dislocation groups, multipoles, and friction stresses in α -CuZn alloys, *Phys. Status Solidi* 109 (1988) 149–160, <https://doi.org/10.1002/pssa.2211090115>.
- [55] J. Plessing, C. Achmus, H. Neuhäuser, B. Schönfeld, G. Kosterz, Short-range order and the mode of slip in concentrated Cu-based alloys, *Zeitschrift Für Met. Res. Adv. Tech.* 88 (1997) 630–635.
- [56] S.J. Sun, Y.Z. Tian, H.R. Lin, H.J. Yang, X.G. Dong, Y.H. Wang, Z.F. Zhang, Transition of twinning behavior in CoCrFeMnNi high entropy alloy with grain refinement, *Mater. Sci. Eng.* 712 (2018) 603–607, <https://doi.org/10.1016/j.msea.2017.12.022>.
- [57] S.W. Wu, G. Wang, J. Yi, Y.D. Jia, I. Hussain, Q.J. Zhai, P.K. Liaw, Strong grain-size effect on deformation twinning of an Al_{0.1}CoCrFeNi high-entropy alloy, *Mater. Res. Lett.* 5 (2017) 276–283, <https://doi.org/10.1080/21663831.2016.1257514>.
- [58] G. Arora, D.S. Aidhy, Machine learning enabled prediction of stacking fault energies in concentrated alloys, *Met.* 10 (2020), <https://doi.org/10.3390/met10081072>.
- [59] A.J. Zaddach, C. Niu, C.C. Koch, D.L. Irving, Mechanical properties and stacking fault energies of NiFeCrCoMn high-entropy alloy, *J. Occup. Med.* 65 (2013) 1780–1789, <https://doi.org/10.1007/s11837-013-0771-4>.
- [60] S. Curtze, V.-T. Kuokkala, A. Oikari, J. Talonen, H. Hänninen, Thermodynamic modeling of the stacking fault energy of austenitic steels, *Acta Mater.* 59 (2011) 1068–1076, <https://doi.org/10.1016/j.actamat.2010.10.037>.
- [61] S. Allain, J.-P. Chateau, O. Bouazziz, A physical model of the twinning-induced plasticity effect in a high manganese austenitic steel, *Mater. Sci. Eng.* 387–389 (2004) 143–147, <https://doi.org/10.1016/j.msea.2004.01.060>.
- [62] L.E. Murr, M.A. Meyers, C.-S. Niou, Y.J. Chen, S. Pappu, C. Kennedy, Shock-induced deformation twinning in tantalum, *Acta Mater.* 45 (1997) 157–175, [https://doi.org/10.1016/S1359-6454\(96\)00145-0](https://doi.org/10.1016/S1359-6454(96)00145-0).
- [63] O. Bouazziz, S. Allain, C.P. Scott, P. Cugy, D. Barbier, High manganese austenitic twinning induced plasticity steels: a review of the microstructure properties relationships, *Curr. Opin. Solid State Mater. Sci.* 15 (2011) 141–168, <https://doi.org/10.1016/j.cossms.2011.04.002>.
- [64] J.-H. Jun, C.-S. Choi, Variation of stacking fault energy with austenite grain size and its effect on the MS temperature of $\gamma \rightarrow \epsilon$ martensitic transformation in Fe–Mn alloy, *Mater. Sci. Eng.* 257 (1998) 353–356, [https://doi.org/10.1016/S0921-5093\(98\)00994-0](https://doi.org/10.1016/S0921-5093(98)00994-0).
- [65] X. An, S. Ni, M. Song, X. Liao, Deformation twinning and detwinning in face-centered cubic metallic materials, *Adv. Eng. Mater.* 22 (2020) 1900479, <https://doi.org/10.1002/adem.201900479>.
- [66] G.B. Olson, M. Cohen, A general mechanism of martensitic nucleation: Part I. General concepts and the FCC \rightarrow HCP transformation, *Metall. Trans. A.* 7 (1976) 1897–1904, <https://doi.org/10.1007/BF02659822>.
- [67] P.J. Ferreira, P. Müllner, A thermodynamic model for the stacking-fault energy, *Acta Mater.* 46 (1998) 4479–4484, [https://doi.org/10.1016/S1359-6454\(98\)00155-4](https://doi.org/10.1016/S1359-6454(98)00155-4).
- [68] A. Saeed-Akbari, J. Imlau, U. Prahl, W. Bleck, Derivation and variation in composition-dependent stacking fault energy maps based on subregular solution model in high-manganese steels, *Metall. Trans. A* (2009) 3076–3090, <https://doi.org/10.1007/s11661-009-0050-8>.
- [69] A.P. Miodownik, The calculation of stacking fault energies in FeNiCr alloys, *Calphad* 2 (1978) 207–226, [https://doi.org/10.1016/0364-5916\(78\)90010-X](https://doi.org/10.1016/0364-5916(78)90010-X).
- [70] J. Nakano, P.J. Jacques, Effects of the thermodynamic parameters of the hcp phase on the stacking fault energy calculations in the Fe–Mn and Fe–Mn–C systems, *Calphad* 34 (2010) 167–175, <https://doi.org/10.1016/j.calphad.2010.02.001>.
- [71] W.S. Yang, C.M. Wan, The influence of aluminium content to the stacking fault energy in Fe–Mn–Al–C alloy system, *J. Mater. Sci.* 25 (1990) 1821–1823, <https://doi.org/10.1007/BF01045392>.
- [72] T. Gao, X. Jin, J. Qiao, H. Yang, Y. Zhang, Y. Wu, Successive strain hardening mechanisms induced by transformation induced plasticity in Fe₆₀Mn₂₀Co₁₀Cr₁₀ high entropy alloys, *J. Appl. Phys.* 129 (2021) 175101, <https://doi.org/10.1063/5.0041352>.
- [73] L. Mosecker, A. Saeed-Akbari, Nitrogen in chromium–manganese stainless steels: a review on the evaluation of stacking fault energy by computational thermodynamics, *Sci. Technol. Adv. Mater.* 14 (2013) 33001, <https://doi.org/10.1088/1468-6996/14/3/033001>.
- [74] A. Dumay, J.-P. Chateau, S. Allain, S. Migot, O. Bouazziz, Influence of addition elements on the stacking-fault energy and mechanical properties of an austenitic Fe–Mn–C steel, *Mater. Sci. Eng. A, Struct. Mater. Prop. Microstruct. Process.* (n.d.) 184–187. doi:DOI:101016/j.msea200612170.
- [75] P. Müllner, P.J. Ferreira, On the energy of terminated stacking faults, *Phil. Mag. Lett.* 73 (1996) 289–298, <https://doi.org/10.1080/095008396180551>.
- [76] T.C. Tisone, The concentration and temperature dependence of the stacking fault energy in face-centered cubic Co–Fe alloys, *Acta Metall.* 21 (1973) 229–236, [https://doi.org/10.1016/0001-6160\(73\)90008-4](https://doi.org/10.1016/0001-6160(73)90008-4).
- [77] H.M. Ledbetter, Poisson's Ratio for Central-Force Polycrystals, *Z. Naturforsch.* 31 1539–21542. doi:https://doi.org/10.1515/zna-1976-1214.
- [78] C. Varvenne, A. Luque, W.A. Curtin, Theory of strengthening in fcc high entropy alloys, *Acta Mater.* 118 (2016) 164–176, <https://doi.org/10.1016/j.actamat.2016.07.040>.
- [79] M.J. Yao, K.G. Pradeep, C.C. Tasan, D. Raabe, A novel, single phase, non-equiatom FeMnNiCoCr high-entropy alloy with exceptional phase stability and tensile ductility, *Scripta Mater.* (2014) 72–73, <https://doi.org/10.1016/j.scriptamat.2013.09.030>, 5–8.
- [80] G. Frommeyer, U. Brux, P. Neumann, Supra-ductile and high-strength manganese-TRIP/TWIP steels for high energy absorption purposes, *ISIJ Int.* 43 (2003) 438–446, <https://doi.org/10.2355/isijinternational.43.438>.
- [81] D. Wei, X. Li, J. Jiang, W. Heng, Y. Koizumi, W.-M. Choi, B.-J. Lee, H.S. Kim, H. Kato, A. Chiba, Novel Co-rich high performance twinning-induced plasticity (TWIP) and transformation-induced plasticity (TRIP) high-entropy alloys, *Scripta Mater.* 165 (2019) 39–43, <https://doi.org/10.1016/j.scriptamat.2019.02.018>.
- [82] K.G. Pradeep, C.C. Tasan, M.J. Yao, Y. Deng, H. Springer, D. Raabe, Non-equiatom high entropy alloys: approach towards rapid alloy screening and property-oriented design, *Mater. Sci. Eng.* 648 (2015) 183–192, <https://doi.org/10.1016/j.msea.2015.09.010>.
- [83] R.L. Fleischer, Solution hardening, *Acta Metall.* 9 (1961) 996–1000, [https://doi.org/10.1016/0001-6160\(61\)90242-5](https://doi.org/10.1016/0001-6160(61)90242-5).
- [84] S. Huang, L.B. T. R. M. M. S. M.E. Vitos, High Entropy Alloys: Elastic Parameters and Trends, Elsevier, 2019, <https://doi.org/10.1016/B978-0-12-803581-8.11714-X>.
- [85] T.B. Massalski, H.W. King, Alloy phases of the noble metals, *Prog. Mater. Sci.* 10 (1963) 3–78.
- [86] H.W. King, *Atomic Volume and Size Correlations in Solid Solutions*, 1965.
- [87] H.W. King, Quantitative size-factors for metallic solid solutions, *J. Mater. Sci.* 1 (1966) 79–90, <https://doi.org/10.1007/BF00549722>.
- [88] V.A. Lubarda, On the effective lattice parameter of binary alloys, *Mech. Mater.* 35 (2003) 53–68, [https://doi.org/10.1016/S0167-6636\(02\)00196-5](https://doi.org/10.1016/S0167-6636(02)00196-5).
- [89] Y.J. Zhao, J.W. Qiao, S.G. Ma, M.C. Gao, H.J. Yang, M.W. Chen, Y. Zhang, A hexagonal close-packed high-entropy alloy: the effect of entropy, *Mater. Des.* 96 (2016) 10–15, <https://doi.org/10.1016/j.matdes.2016.01.149>.
- [90] H. Yao, J.-W. Qiao, M.C. Gao, J.A. Hawk, S.-G. Ma, H. Zhou, MoNbTaV medium-entropy alloy, *Entropy* 18 (2016), <https://doi.org/10.3390/e18050189>.
- [91] H.W. Yao, J.W. Qiao, J.A. Hawk, H.F. Zhou, M.W. Chen, M.C. Gao, Mechanical properties of refractory high-entropy alloys: experiments and modeling, *J. Alloys Compd.* 696 (2017) 1139–1150, <https://doi.org/10.1016/j.jallcom.2016.11.188>.
- [92] Y. Zhang, T.T. Zuo, Z. Tang, M.C. Gao, K.A. Dahmen, P.K. Liaw, Z.P. Lu, Microstructures and properties of high-entropy alloys, *Prog. Mater. Sci.* 61 (2014) 1–93, <https://doi.org/10.1016/j.pmatsci.2013.10.001>.
- [93] T. Rieger, J.-M. Joubert, M. Laurent-Brocq, L. Perrière, I. Guillot, J.-P. Couzinié, Study of the FCC+L12 two-phase region in complex concentrated alloys based on the Al–Co–Cr–Fe–Ni–Ti system, *Materialia* 14 (2020) 100905, <https://doi.org/10.1016/j.mtla.2020.100905>.
- [94] B.B. Bian, N. Guo, H.J. Yang, R.P. Guo, L. Yang, Y.C. Wu, J.W. Qiao, A novel cobalt-free FeMnCrNi medium-entropy alloy with exceptional yield strength and ductility at cryogenic temperature, *J. Alloys Compd.* 827 (2020) 153981, <https://doi.org/10.1016/j.jallcom.2020.153981>.
- [95] Y. Wu, X. Jin, M. Zhang, H. Yang, J. Qiao, Y. Wu, Yield strength-ductility trade-off breakthrough in Co-free Fe₄₀Mn₁₀Cr₂₅Ni₂₅ high-entropy alloys with partial recrystallization, *Mater. Today Commun.* 28 (2021) 102718, <https://doi.org/10.1016/j.mtcomm.2021.102718>.
- [96] M.S. Mehranpour, H. Shahmir, M. Nili-ahmadabadi, CoCrFeNiMn high entropy alloy microstructure and mechanical properties after severe cold shape rolling and annealing, *Mater. Sci. Eng.* 793 (2020) 139884, <https://doi.org/10.1016/j.msea.2020.139884>.
- [97] M. V. Klimova, D.G. Shaysultanov, S. V. Zherebtsov, N.D. Stepanov, Effect of second phase particles on mechanical properties and grain growth in a CoCrFeMnNi high entropy alloy, *Mater. Sci. Eng.* 748 (2019) 228–235, <https://doi.org/10.1016/j.msea.2019.01.112>.